Views of Earth's Magnetosphere with the IMAGE Satellite

J. L. Burch,[1*] S. B. Mende,[2] D. G. Mitchell,[3] T. E. Moore,[4] C. J. Pollock,[1] B. W. Reinisch,[5] B. R. Sandel,[6] S. A. Fuselier,[7] D. L. Gallagher,[8] J. L. Green,[4] J. D. Perez,[9] P. H. Reiff[10]

The IMAGE spacecraft uses photon and neutral atom imaging and radio sounding techniques to provide global images of Earth's inner magnetosphere and upper atmosphere. Auroral imaging at ultraviolet wavelengths shows that the proton aurora is displaced equatorward with respect to the electron aurora and that discrete auroral forms at higher latitudes are caused almost completely by electrons. Energetic neutral atom imaging of ions injected into the inner magnetosphere during magnetospheric disturbances shows a strong energy-dependent drift that leads to the formation of the ring current by ions in the several tens of kiloelectron volts energy range. Ultraviolet imaging of the plasmasphere has revealed two unexpected features—a premidnight trough region and a dayside shoulder region—and has confirmed the 30-year-old theory of the formation of a plasma tail extending from the duskside plasmasphere toward the magnetopause.

The IMAGE (Imager for Magnetopause-to-Aurora Global Exploration) spacecraft was launched on 25 March 2000 into an elliptical polar orbit (apogee altitude = 7.2 Earth radii; perigee altitude = 1000 km) (*1*). The IMAGE instruments image the tenuous plasmas that populate the inner regions of Earth's magnetosphere, which is the region of space dominated by the geomagnetic field and shielded by it from the solar wind. The interaction between the solar wind, with its embedded interplanetary magnetic field, and Earth's magnetic field results in the transfer of energy, momentum, and mass to the magnetosphere and drives the large-scale flow of plasma within it. The energy thus transferred accumulates in the magnetotail, the portion of the magnetosphere on Earth's night side that is drawn out like the tail of a comet by solar wind flow, until it is released explosively in a process known as a magnetospheric substorm (*2*). Such events involve a change in the morphology of the geomagnetic field from a stretched configuration to a more dipolar one and the acceleration of plasma flows toward and away from the planet. Substorms are associated with changes in the morphology and brightness of the aurora.

The energy transfer from the solar wind to the magnetosphere can continue over an extended period of time, several hours to days, resulting in a sustained enhancement of the large-scale sunward flow of plasma from the magnetotail toward the dayside magnetosphere. Such periods of sustained plasma circulation are known as geomagnetic storms and are characterized by the growth of the ring current (an east-west current encircling Earth at geocentric distances between 2 and 6 Earth radii and carried by trapped energetic charged particles) and by the occurrence of multiple substorms (*3*). Geomagnetic storms can occur at any time during the 11-year solar cycle, but occur most frequently around solar maximum and are often triggered by the arrival at Earth of coronal mass ejections and the associated shocks.

Our picture of the dynamics and changing structure of the inner magnetosphere during substorms and geomagnetic storms is largely a statistical one, based on data acquired by single spacecraft at single points in space at different times and on the results of numerical simulations. However, placing this picture on a solid observational footing and testing and validating the results of our models require that we image, on a global scale and with a temporal resolution of minutes, the coupled interactions of the different inner magnetospheric plasma populations as they process and redistribute the energy received from the solar wind. Here we present global images of Earth's inner magnetosphere as seen with instruments on board the IMAGE spacecraft during the geomagnetic storms of 24 May and 8 June 2000 and during a substorm that occurred on 10 June 2000.

Experimental Techniques

Magnetospheric plasmas are invisible to standard astronomical observing techniques, although their properties can be determined through in situ measurement. To obtain the necessary global images, IMAGE uses three different and innovative imaging technologies that allow these plasmas to be sensed remotely: neutral atom imaging, ultraviolet (UV) imaging, and radio sounding. Three neutral atom imagers, covering the low (10 eV to 1 keV) (*4*), medium (1 to 30 keV) (*5*), and high (20 to 500 keV) (*6*) energy ranges, detect energetic neutral atoms (ENAs) produced by charge-exchange reactions between magnetospheric ions and the hydrogen atoms of Earth's exosphere (the high-altitude extension of the neutral atmosphere). Unlike the parent ions, the ENAs are not constrained by the geomagnetic field and can travel in line-of-sight paths to the imagers aboard the spacecraft, making it possible to construct images of the ion source populations. Neutral atom imaging is used to image the ring current, the inner edge of the plasma sheet, and outflowing ionospheric plasma. The second technique used by IMAGE is the detection of extreme ultraviolet (EUV) solar photons (wavelength λ = 30.4 nm) resonantly scat-

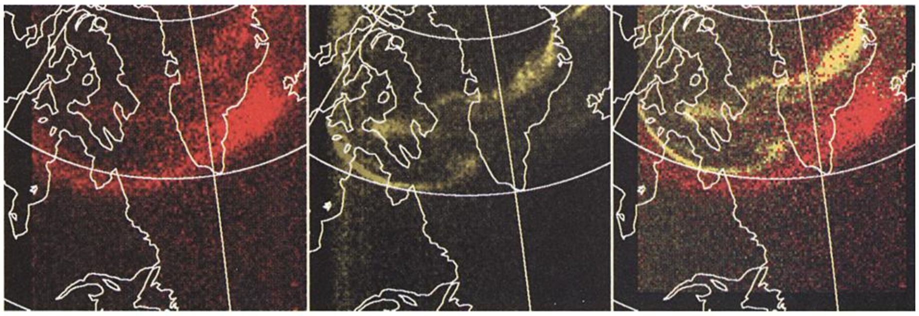

Fig. 1. Partial picture of the auroral oval on 16 June 2000 at 22:49 UT, with overlaid continental outlines and geographic grid. Simultaneous images from the FUV SI12 and SI13 channels show auroral emissions from proton precipitation (red) and electron precipitation (yellow). The images from both channels (right) are overlaid to highlight the differing morphology and spatial distribution of the proton and electron auroras.

[1]Southwest Research Institute, Post Office Drawer 28510, San Antonio, TX 78228, USA. [2]Space Sciences Laboratory, University of California Berkeley, Berkeley, CA 94720, USA. [3]Johns Hopkins University Applied Physics Laboratory, Laurel, MD 20723, USA. [4]NASA–Goddard Space Flight Center, Greenbelt, MD 20771, USA. [5]Center for Atmospheric Research, University of Massachusetts, Lowell, MA 01854, USA. [6]Lunar and Planetary Laboratory, University of Arizona, Tucson, AZ 85721, USA. [7]Lockheed Martin Advanced Technology Center, Palo Alto, CA 94304, USA. [8]NASA–Marshall Space Flight Center, Huntsville, AL 35812, USA. [9]Physics Department, Auburn University, Auburn, AL 36849, USA. [10]Physics and Astronomy Department, Rice University, Houston, TX 77005, USA.

*To whom correspondence should be addressed. E-mail: jburch@swri.edu

tered by singly ionized helium atoms in Earth's plasmasphere (*7*). The plasmasphere is a doughnut-shaped region of cold (~1 eV), dense (10^3 cm^{-3}) plasma of ionospheric origin that surrounds and corotates with Earth. It is composed largely of protons but has a helium ion component that accounts for 10 to 15% of the total plasmaspheric density (*8*). The third imaging technique used on IMAGE is radio sounding of plasma gradients and boundaries (*9*). In addition to the instruments using these three techniques, IMAGE carries far-ultraviolet (FUV) imaging instruments that provide highly resolved wideband images of the aurora (*10–12*). Auroral imaging provides a diagnostic of the dynamic state of the magnetosphere.

Global Imaging of the Proton Aurora

The IMAGE FUV imager takes global images of the aurora in three different wavelength channels: (i) broadband N_2 Lyman-Birge-Hopfield emissions in the wavelength range 140 to 190 nm, (ii) narrowband (4 nm wide) OI line emissions at 135.6 nm, and (iii) a number of selected narrow bands (~0.1-nm each) in the vicinity of the Lyman alpha (Ly-α) line of hydrogen (121.6 nm). The broadband images are obtained by the wideband imaging camera (WIC), whereas the narrowband images are recorded through the two wavelength channels (SI12 and SI13) of the spectrographic imager (SI). The SI12 channel is designed to image fast hydrogen atoms with Doppler-shifted Ly-α, thus obtaining global images of the proton aurora. The SI is a grating-based instrument that minimizes throughput at Ly-α (121.6 nm) and at other auroral nitrogen and oxygen emission lines, while maximizing throughput at 121.8 nm, which is emitted by hydrogen atoms traveling away from the imager at energies of about 8 keV. As energetic protons precipitate into the atmosphere and collide with the atmospheric gases, they capture electrons from the neutral constituents (such as N_2, O_2, and O) through charge-exchange reactions. The protons are thus converted into fast neutral hydrogen atoms, which emit Ly-α radiation through resonant scattering of solar Ly-α. Subsequently, the hydrogen atoms may be converted back to protons and continue their motion along the magnetic field into the atmosphere only to be converted again to hydrogen atoms, with the process repeating itself perhaps thousands of times.

Because the Ly-α radiation from Earth's geocorona (*13*) is at least 100 times more intense than the proton aurora, an imager with very high spectral resolution is required. By observing the Doppler-shifted Ly-α, IMAGE FUV observes the actual precipitating particles (fast hydrogen atoms), unlike the other channels and all previously flown auroral imagers, which observe the atmospheric glow created by the energy input of the auroral particles into the atmosphere.

The dynamics of the aurora, especially the development of auroral substorms, has been studied extensively by ground-based techniques and by FUV auroral imagers flown on previous spacecraft missions (*14–17*). These imagers detected atmospheric emissions produced almost exclusively by precipitating electrons. Until now relatively little progress has been made in describing the global dynamics of proton precipitation even though protons carry by far the largest fraction of the particle energy in the magnetosphere. The ring current consists mainly of stably trapped protons (*18*), but a fraction of the trapped energetic protons are scattered out of their trapped orbits by wave-particle interactions and precipitate into the atmosphere, causing the proton aurora. Although the largest fraction of the precipitating energy into the aurora is carried by electrons, there are regions in which protons represent the major source of auroral energy into the atmosphere (*19*).

Even though proton precipitation is an important energy input to the upper atmosphere, the global distribution of the proton aurora is not known. In models, the electron and proton ovals are assumed to be symmetric and located at the same position (*19*). What knowledge there is about the global distribution of proton auroras comes from statistical patterns of proton precipitation, which show that the proton oval is shifted equatorward from the electron oval before midnight and poleward of it after midnight (*20*). With IMAGE, the proton oval can finally be seen (Fig. 1). The SI13 image shows auroral atmospheric emissions, which are caused by electrons and some protons. These auroras show a diffuse band at lower latitudes and narrow structures at higher latitudes. The SI12 image shows only diffuse auroral emissions, which are produced overwhelmingly by protons during that part of their lifetime when they exist as charge-exchanged hydrogen atoms. The third image shows that both electron and proton auroras contain a diffuse band at lower latitudes, but the highly structured auroras seen at higher latitudes are for the most part caused by electron precipitation. The image set shown is a typical example of nightside auroral behavior during a post substorm-onset period. From such examples we can observe directly that large poleward expansion of the aurora affects only the electrons, and the high-latitude discrete auroras rarely contain any protons.

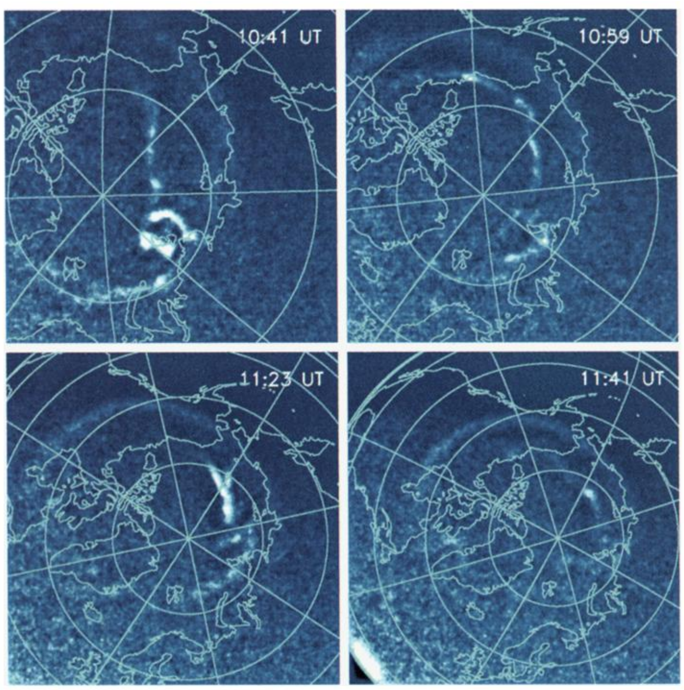

Fig. 2. FUV WIC images from 10 June 2000 for the period 10:41 to 11:41 UT, showing the latter part of a period of substorm activity and the subsequent recovery. Auroral images are obtained every 2 min by the FUV instrument. Here four representative images are shown, which suffice to follow the development and recovery of auroral activity during this period. The prime meridian extends from the pole to the lower left quadrant of each image. Along this meridian the universal time (UT) labeled in each figure is equal to the local time. Circles of geographic latitude are shown every 10°. Dayglow emissions (resulting from the interaction between neutral atoms and molecules and photoelectrons produced by solar EUV and x-ray emissions) have been substracted with the method of Immel *et al.* (*32*).

Substorm Plasma Injection

Models of magnetospheric substorm onset identify the development of a region of magnetic reconnection at geocentric distances of about 20 Earth radii down the geomagnetic tail and an associated region of neutral sheet current disruption closer to Earth at 6 to 10 Earth radii (*21*). Mechanisms for the current disruption have not been identified, but the effect has been observed as a rapid dipolarization of the magnetic field from an initial stretched configuration. This dipolarization is accompanied by the injection of plasma from the plasma sheet toward Earth. The plasma injection, which typically moves across geosynchronous orbit in the equatorial plane, is associated with rapid intensification of the discrete aurora near its equatorward edge. Subsequently, the aurora becomes active, spreads poleward, and often develops a feature known as the westward traveling surge, which moves rapidly from midnight toward the dusk meridian. Although the global auroral forms have been imaged before, the plasma injection and subsequent transport in the inner magnetosphere have had to be modeled from localized in situ measurements of the plasma. With IMAGE, the plasma injection and transport associated with substorms is being imaged repeatedly by neutral atom imagers. Energetic neutral atom images have previously been obtained during substorms by an energetic ion detector on the Polar spacecraft (*22*, *23*). During those times when Polar was in the polar cap region, in which ion fluxes were generally below the instrument threshold, the observed signals were primarily due to neutral atoms. These previous measurements were an important precursor to the higher resolution and wider energy-range neutral atom imaging now being performed by IMAGE. Whereas the neutral atom images obtained with the IMAGE ENA instruments provide global measurements of the ion distributions, the production of ion images requires image inversion (*24*, *25*), which takes advantage of the on-board measurement of the exospheric hydrogen atom densities using their UV emissions.

A series of UV auroral images from FUV-WIC (Fig. 2) records the auroral activity during a substorm on 10 June 2000 and its subsequent recovery. Ground magnetic records and images from the Ultraviolet Imager on the Polar satellite (*17*) show a substorm intensification at 09:18 UT. The FUV WIC camera began imaging the aurora at 10:15 UT after a perigee pass of the IMAGE satellite, during which global auroral viewing was not possible. The subsequent series of images tracked the last part of the extended substorm activity on 10 June and the period of recovery. Six ENA images from the IMAGE MENA (*5*) and HENA (*6*) instruments (Fig. 3) show the evolution of the inner magnetosphere during this same period of substorm activity and recovery. At 11:00 UT, when the auroral emissions are still rather intense (as shown in Fig. 2), strong ENA emissions in the lowest energy range (Fig. 3A) are seen to cover most of the nightside hemisphere. At higher energies (Fig. 3B), the substorm-injected ions have drift-

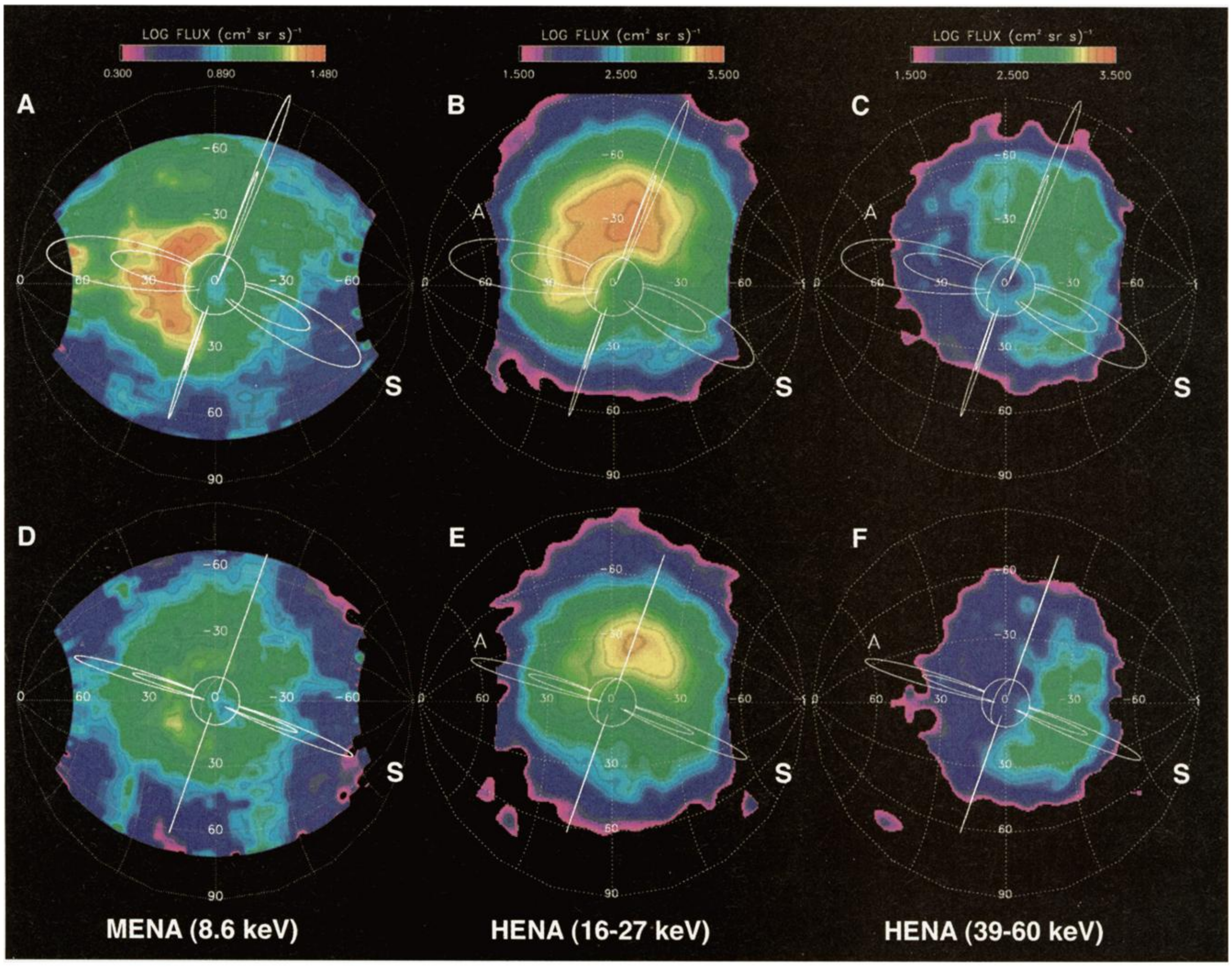

Fig. 3. MENA and HENA images from 10 June 2000 at 11:00 UT (top row) and 11:40 UT (bottom row). The view is from above the north pole at geocentric distances of about 4 and 5 Earth radii for the top and bottom rows, respectively. The top row (**A** to **C**) is during the late stages of a substorm, which began at 09:18 UT, whereas the bottom row (**D** to **F**) is well into its recovery. Although the images are produced every 2 min, 6-min averaged images, representing data from three successive spin periods of the spacecraft, are presented. Each row contains an 8.6-keV neutral atom image from MENA, a 16- to 27-keV image from HENA, and a 39- to 60-keV image from HENA. In each image the white circle represents Earth, upon which the terminator is shown. Two magnetic field lines with equatorial intersections at 4 and 8 Earth radii, respectively, are shown at noon, midnight, dawn, and dusk local times. The noon field lines are noted with an S (sun), and the midnight field lines by A (anti-sun). The MENA images have a horizontal field of view of 120°; the vertical field of view is limited by an on-board program to 90° of spin phase centered on Earth. The MENA color bar is presented in terms of count rate. The HENA images are similar except that the width is 107°, the height is 100°, and the color bar is presented in terms of neutral atom flux. Earth appears smaller in the bottom row because the spacecraft increased its altitude between 11:00 and 11:40 UT.

ed well beyond the dusk meridian, while at still higher energies (39 to 60 keV), the leading edge of the substorm ion population has drifted beyond the noon meridian (Fig. 3C).

By 11:40 UT, the overall ENA signal has diminished at the lower energies (Fig. 3D), whereas the higher energy particle fluxes remain relatively strong (Fig. 3, E and F) and the higher energy particles have drifted farther around Earth, reaching the dawn meridian (Fig. 3F). Because all of the global auroral imaging that has previously been performed in the magnetosphere was of the electron aurora, it has not been known exactly where the injected ions are transported and precipitated. The ENA images (Fig. 3) show that ions with energies of several keV remain mostly within the nightside hemisphere. The higher energy particles (several tens of keV) drift rapidly through the dusk hemisphere and into the morning hours, and their fluxes remain strong even after the substorm subsides. The drift period for 50-keV protons in a dipole field at a radial distance of 4 Earth radii is 3.4 hours. Comparison of the 39- to 60-keV ENA data from the two times (11:00 and 11:40 UT) shows that this result is roughly consistent with the drift motion of the cloud of ENA emissions.

In evaluating the ENA images it is important to note that the measured ENAs are those with velocities directed toward the spacecraft so that the relative geometry of the viewing aspect and the geomagnetic field causes the signals from certain regions to be enhanced over others. In addition, the concentration of atmospheric hydrogen atoms near Earth, combined with the focusing action of Earth's nearly dipolar magnetic field lines, causes the ENA signal to be enhanced at low altitudes. Such effects can be reduced by an image inversion process that converts the ENA images into ion images (*24*, *25*). Such a process (*25*) has been applied to the HENA data from 10 June (Fig. 3, B and C, E and F). The image inversion results yield the spatial distribution in the equatorial plane of the ion flux integrated over the line of sight (Fig. 4).

Development of the Ring Current

A geomagnetic storm occurred on 24 May 2000, with a drop in the surface magnetic field strength of 147 nT during the storm's main phase, as measured by the Dst, or disturbed storm time index. The build-up of the ring current, which was responsible for the magnetic perturbations felt on Earth during this storm, can be seen in images from the HENA instrument (*6*) (Fig. 5). Previously, energetic neutral atoms were detected with ion detectors on the ISEE-1 and IMP 7/8 spacecraft (*26*), and an ENA image was constructed from the ISEE-1 measurements (*27*). Those measurements provided an important baseline for the design of the HENA instrument. The IMAGE HENA data for this storm show two particularly noteworthy features. First, the ENA emission is at its maximum from low altitudes, at the footpoints of the magnetic field lines, and this feature is confined to the night side of Earth. Farther from Earth on the day side, a distinct region of ENA emission from the ring current peaks between about $L = 3$ and $L = 4$. Whereas the outer extent of this emission is limited by the steep radial decline in geocoronal density, the drop at the inner edge must be dominated by the contours of the parent-ion distribution. Second, this peak in the ring current distribution is asymmetric. It does not completely surround Earth; rather, it is strong only in the dusk-noon quadrant and decays quickly between noon and dawn. This second feature is energy-dependent, as shown by a comparison of HENA data for two different energy ranges, 16 to 27 keV (Fig. 5A) and 27 to 60 keV (Fig. 5B). The higher-energy data show a partial ring current that is much more distinct, and more strongly confined to the quadrant about the noon meridian, than is the lower-energy population, demonstrating that the ring current ion distribution is a strong function of energy during the main phase of this storm.

The ENA data for the 24 May storm (Fig. 5) show the strongest ENA emissions coming from the auroral regions close to Earth. This observation is consistent with the substorm conditions that existed at the time the images were made. On the other hand, observations of the ring current during quiet periods between substorms shows that the ENA emissions from low altitudes are reduced to low levels, and that the strongest emissions come from the equatorial ring current. For example, HENA data acquired during the recovery phase of a modest magnetic storm on 8 to 9 June 2000 (Fig. 6) reveal a distinct ring-shaped maximum in the ENA emission, with a low-emission region (down by about a factor of 2) in the dawn-midnight quadrant. The emission from the footpoints of the field lines, where the ions enter the dense atmosphere, is relatively low. Because the neutral gas density is highest at the magnetic field footpoints, the low ENA flux from that region implies that the ion fluxes are also low. This conclusion must be qualified by the understanding that from the observing posi-

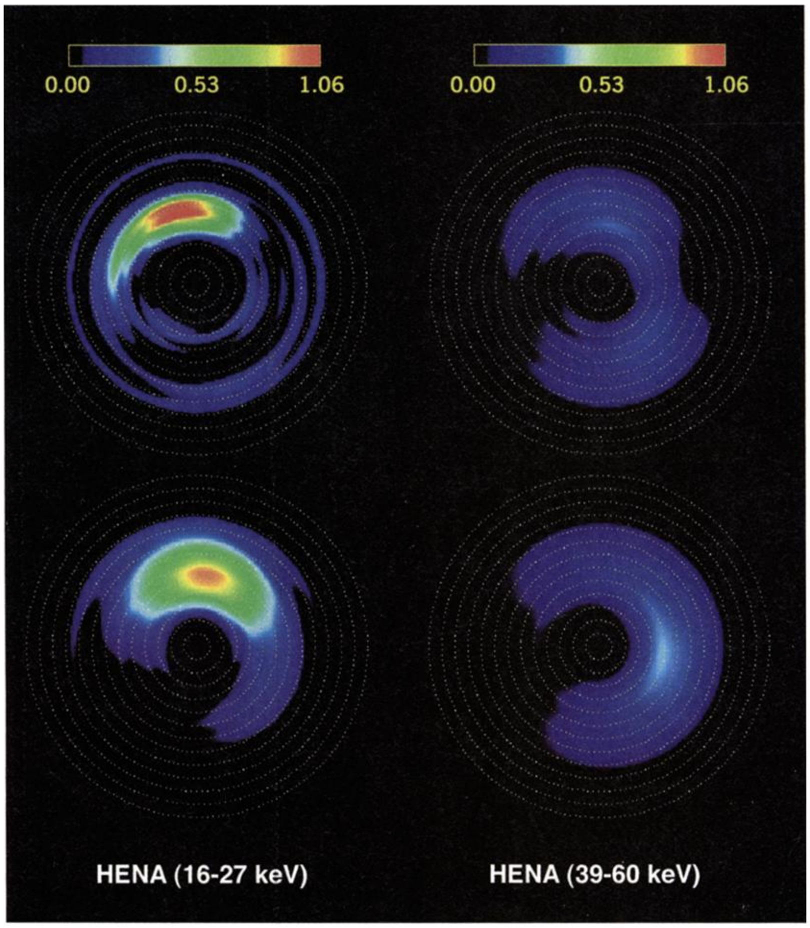

Fig. 4. Results of an image inversion (*25*) applied to the HENA data for 11:00 (top row) and 11:40 UT (bottom row) on 10 June (Fig. 3). Plotted is total ion flux integrated over magnetic pitch angle in the equatorial plane. The view is from above the north pole toward the equatorial plane. The dotted lines are 1 Earth radius apart.

tion of the spacecraft at the time the data were taken, ENA emission from the field footpoints would only be produced by the interaction between upward-flowing energetic ions and the upper atmosphere. Because during relatively quiet times the energetic ion population moving parallel to the magnetic field is typically depleted by collisions with the atmosphere, it is no surprise that this emission is low. Any ENAs originating from these regions would have to be scattered (either as ions or neutrals) into the upward-going direction through collisions and escape the atmosphere before they lose all of their energy.

Dynamical Response of the Plasmasphere to Magnetic Storms

Cold plasma from the ionosphere flows outward along magnetic field lines, where it accumulates. This accumulation creates a roughly doughnut-shaped region that encircles Earth at the magnetic equator and is called the plasmasphere (*28*). Nearest Earth, planetary rotation generates an inward-directed radial electric field that causes plasmaspheric plasma to corotate with Earth. At greater distances, a dawn-to-dusk directed electric field generated by the solar wind flow through the outer magnetosphere dominates plasmaspheric motion. Depending on the strength of the interaction between the solar wind and Earth's magnetic field, this electric field penetrates into the magnetosphere, causing a flow of plasma perpendicular to both the electric field and the geomagnetic field and directed toward the dayside magnetospheric boundary. Plasma caught up in this sunward flow does not accumulate; instead, it is carried to the dayside magnetopause where it is assumed to be lost. The boundary-like transition between the high-density inner region and the lower-density outer region is called the plasmapause (*29*).

During magnetic storms, the electric field induced by the solar wind becomes stronger, penetrating into dense plasma within the plasmasphere. Instead of continuing to drift around Earth, these outer plasma shells are drawn away from the plasmasphere. This plasmaspheric erosion is accompanied by the injection of energetic plasma from the magnetospheric tail, which becomes the ring current. Owing to actions of the convection, corotation, interactions with the ring current, and continued ionospheric outflow, plasmaspheric plasma is seen throughout the inner magnetosphere and beyond to the dayside magnetopause. Modeling of these processes suggests that plasmaspheric erosion results in an extended tail of cold plasma extending from the plasmasphere outward in the local afternoon to the dayside magnetopause, especially during magnetic storm times (*30*, *31*).

With IMAGE we can begin to assemble a global description of plasmaspheric structure, of its motion, and of the physical processes

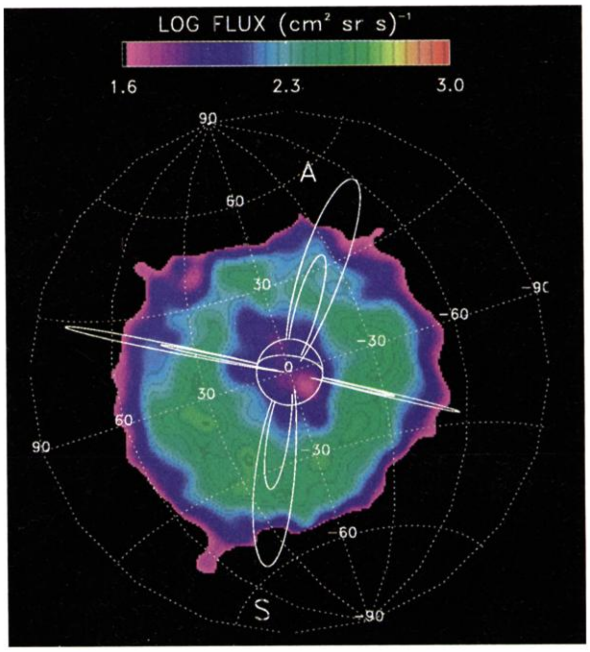

Fig. 6. ENA emission as seen with the IMAGE/HENA instrument from 5.0 Earth radii above the north magnetic pole during the geomagnetic storm of 8 to 9 June 2000. The image shows the ring current at 21:18 UT on 9 June during the later stages of the storm, when the Dst had recovered to −26 nT from a main phase Dst of −87 nT at 20:00 UT on 8 June. In the image, the Earth's disk is inscribed, along with representative dipole magnetic field lines at $L = 4$ and 8 for the sunward (down), dawn (left), midnight (up), and dusk (right) merdians. The terminator (great circle separating day from night) is also drawn onto the Earth disk for reference. The ENA emission is integrated over an energy range from 27 to 60 keV. (The ENAs are assumed to be hydrogen, because the HENA instrument does not identify the ENA species in the mode for which these data were taken.)

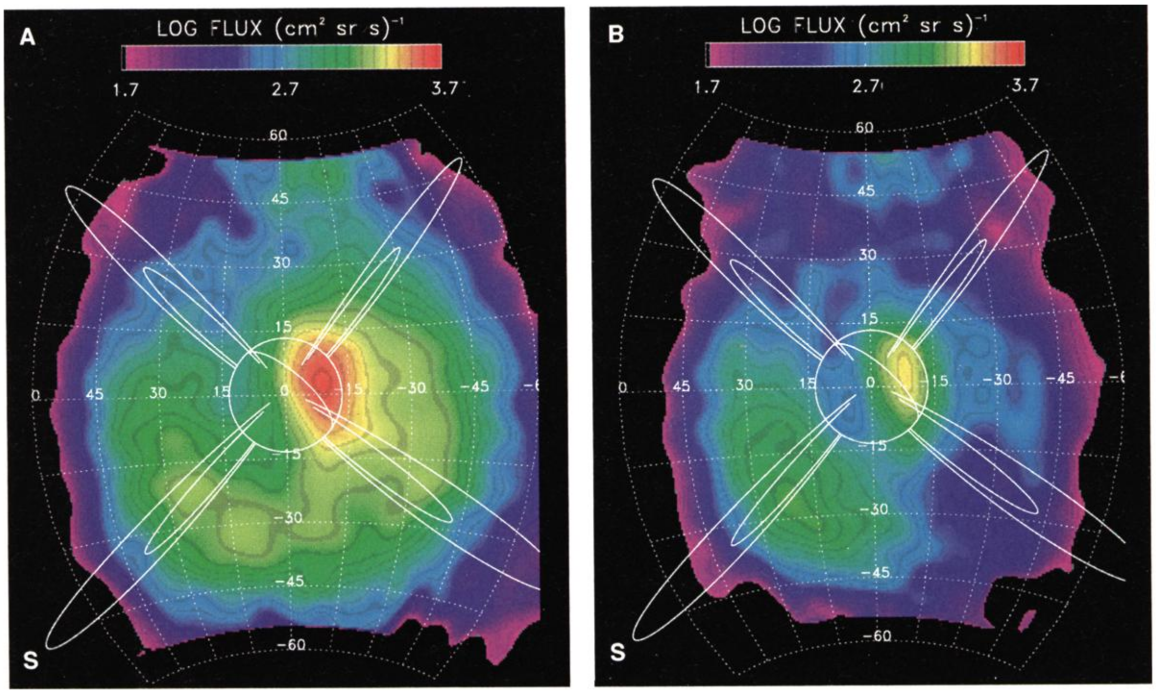

Fig. 5. ENA images of the ring current during the main phase of a geomagnetic storm on 24 May 2000. Data for two energy ranges are shown: 16 to 27 keV (**A**) and 39 to 60 keV (**B**). The view is from about 4.3 Earth radii above the north magnetic pole. The sun (S) is toward the lower left. The enhanced emission at the upper edge of both images is an instrument artifact and should be ignored. The images were produced by integrating the ENA counts over 6 min (three spacecraft spin periods), from 06:18:51 to 06:24:49 UT.

that dominate its behavior. As noted above, EUV light from the sun is absorbed and reemitted by helium ions, making the plasmasphere luminous in 30.4-nm light. The EUV instrument (*7*) on IMAGE is able to selectively see light at this wavelength and returns global images of the plasmasphere (Fig. 7), making it possible to identify and follow the pattern of plasmaspheric ebb and flow throughout the inner magnetosphere with a global image every 10 min.

Six EUV images beginning near the main phase of the 24 May 2000 magnetic storm and extending over the next 3 hours show a changing distribution of plasmaspheric plasma during a magnetospheric disturbance (Fig. 7) and reveal a global pattern of behavior only hinted at in previous single- or multipoint studies. With the sun located off to the lower right, Earth's shadow in UV light can be seen in these images extending up and to the left. In the premidnight sector of the plasmasphere, just to the right and extending away from the shadow is a narrow channel mostly emptied of plasma. "Bite outs" of plasma have been measured previously by ground-based radio techniques and by orbiting spacecraft, but we have never known the longitudinal extent or the cause of these features.

The images also reveal what appears to be a plasmaspheric "shoulder," where the plasmapause position moves outward abruptly as it is traced toward earlier local times in the dawn hemisphere. Comparison of the location of this shoulder in the six images shows it to be nearly corotating with Earth. The apparent shape of the shoulder also evolves from rounded (in the first image) to very sharp (in the final image). This evolution in shape may be due to the change in perspective from a side view (at a large angle to the plane of the nearly dipolar magnetic field lines) to a top view (looking parallel to the plane of the field lines). At this point there is no clear explanation for this feature, which has been seen in several EUV images acquired during magnetic storms.

The EUV images from 24 May also show the predicted plasmaspheric tail (*31*) formed by solar wind–driven convection. The tail connects to the main body of the plasmasphere in the afternoon/dusk sector and extends toward the sun. The overall motion of plasmaspheric plasma is dominated by electric fields generated by Earth's rotation and by the solar wind. However, these electric fields are poorly known near Earth at low magnetic latitudes. This region is characterized by the intermingling of hot plasmas injected from the tail with cooler plasmaspheric plasma. Wave-particle interactions, mesoscale electric fields due to charge separation, and a variety of other physical processes are thought to cause cross-field diffusion, heating, and localized enhanced convection. By following features observed at the relatively high resolution (0.6° by 0.6°) of the EUV instrument, it is possible to map electric fields throughout the inner magnetosphere. Details of the penetration of the global convection electric field, the importance of ionospheric conductivity, and the impact of mesoscale physical processes on plasma and energy transport can all be studied by the global mapping of electric fields.

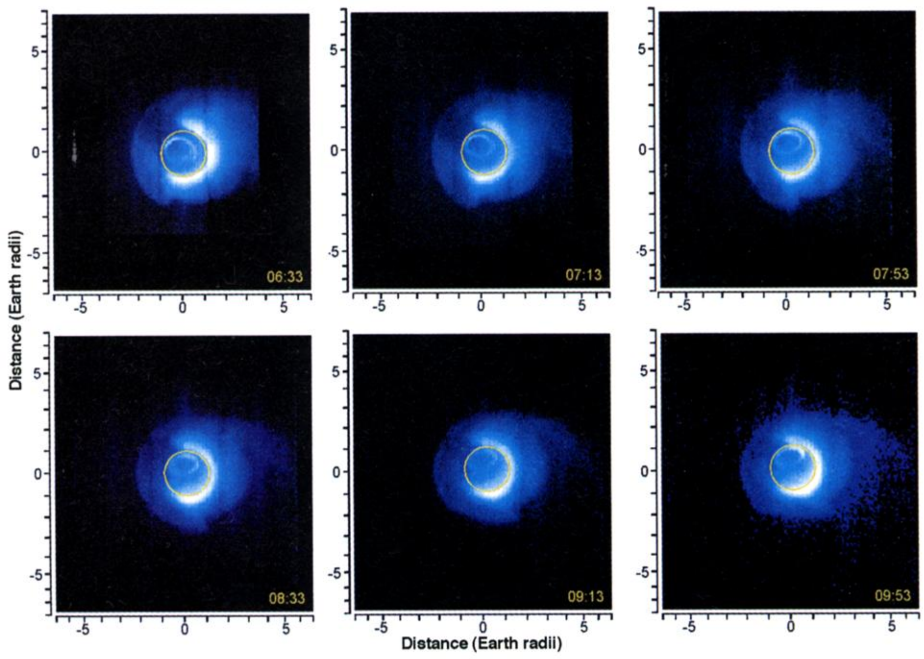

Fig. 7. Extreme ultraviolet emissions from the plasmasphere as imaged by the EUV instrument from above the northern polar cap during a magnetic storm on 24 May 2000. The first image was acquired near the peak of the storm, at about the same time as the HENA images shown in Fig. 5. During the 3-hour period covered by the images, the spacecraft was rising above the Northern Hemisphere. The view is from Earth's morning side toward the north magnetic pole. The yellow circle indicates Earth. The sun is to the lower right corner of each image, opposite the dark shadow region. Notable in each image are the northern EUV aurora, most likely from excitation of O^+ with an emission line at 53.9 nm; a bright dayside emission, which is at least partially due to 58.4-nm emissions from the helium geocorona; a narrow ion trough extending from the shadow region toward the dusk meridian; a plasma tail that develops in the duskside hemisphere; and a sharp discontinuity, or shoulder, in the outer boundary of the plasmasphere in the morning hours. Each image pixel is an integral of the EUV volume emission rate along the corresponding line of sight. The volume emission rate is proportional to the local He^+ density.

References and Notes

1. J. L. Burch, *Space Sci. Rev.* **91**, 1 (2000).
2. S.-I. Akasofu, *Polar and Magnetospheric Substorms* (Reidel, Dordrecht, Netherlands, 1968).
3. B. T. Tsurutani, W. D. Gonzalez, Y Kamide, J. K. Arballo, Eds., *Magnetic Storms* (Geophysical Monograph 98, American Geophysical Union, Washington, DC, 1997).
4. T. E. Moore *et al.*, *Space Sci. Rev.* **91**, 155 (2000).
5. C. J. Pollock *et al.*, *Space Sci. Rev.* **91**, 113 (2000).
6. D. G. Mitchell *et al.*, *Space Sci. Rev.* **91**, 67 (2000).
7. B. R. Sandel *et al.*, *Space Sci. Rev.* **91**, 197 (2000).
8. R. R. Meier *et al.*, *J. Geophys. Res.* **103**, 17505 (1998).
9. B. W. Reinisch *et al.*, *Space Sci. Rev.* **91**, 319 (2000).
10. S. B. Mende *et al.*, *Space Sci. Rev.* **91**, 243 (2000).
11. S. B. Mende *et al.*, *Space Sci. Rev.* **91**, 271 (2000).
12. S. B. Mende *et al.*, *Space Sci. Rev.* **91**, 287 (2000).
13. R. L. Rairden *et al.*, *J. Geophys. Res.* **91**, 13613 (1986).
14. L. A. Frank, J. D. Craven, *Rev. Geophys.* **26**, 249 (1988).
15. C. D. Anger *et al.*, *Geophys. Res. Lett.* **14**, 387 (1987).
16. J. S. Murphree *et al.*, *Space Sci. Rev.* **70**, 421 (1994).
17. G. A. Germany *et al.*, *Geophys. Res. Lett.* **24**, 995 (1997).
18. D. J. Williams, *Rev. Geophys.* **25**, 570 (1987).
19. M. Galand *et al.*, *J. Geophys. Res.* **104**, 27,973 (1999).
20. D. A. Hardy *et al.*, *J. Geophys. Res.* **94**, 370 (1989).
21. D. N. Baker *et al.*, *J. Geophys. Res.* **98**, 3815 (1993).
22. M. G. Henderson *et al.*, *Adv. Space Res.* **25**, 2407 (2000).
23. A. M. Jorgensen *et al.*, *J. Geophys. Res.* **105**, 18753 (2000).
24. E. C. Roelof, A. J. Skinner, *Space Sci. Rev.* **91**, 437 (2000).
25. J. D. Perez *et al.*, *Space Sci. Rev.* **91**, 421 (2000).
26. E. C. Roelof *et al.*, *J. Geophys. Res.* **90**, 10,991 (1985).
27. E. C. Roelof, *Geophys. Res. Lett.* **14**, 652 (1987).
28. C. R. Chappell *et al.*, *J. Geophys. Res.* **75**, 3848 (1970).
29. D. L. Carpenter, *J. Geophys. Res.* **71**, 693 (1966).
30. J. M. Grebowsky, *J. Geophys. Res.* **75**, 4329 (1970).
31. A. J. Chen *et al.*, *J. Geophys. Res.* **80**, 968 (1975).
32. T. Immel *et al.*, *JATSP* **62**, 47 (2000).
33. We thank W. Lewis, J. Micha-Jahn, R. Gladstone, and E. Mayfield (Southwest Research Institute) for preparation of the figures. We are grateful to the IMAGE investigators who participated in the analysis of data for this paper. These scientists include H. Frey and T. Immel (University of California, Berkeley); B. Giles, S. Fung, and M. Collier (NASA-Goddard Space Flight Center); P. Brandt (Johns Hopkins Applied Physics Laboratory); and R. King and C. Curtis (University of Arizona). We appreciate the Polar UVI data provided by M. Brittnacher (University of Washington). Supported by NASA Contract No. NAS5-96020 with Southwest Research Institute.

10 October 2000; accepted 13 December 2000